Interplay of rare-earth and transition-metal subsystems in $Cu_3Yb(SeO_3)_2O_2Cl$

M. M. Markina,[1] K. V. Zakharov,[1] E. A. Ovchenkov,[1] P. S. Berdonosov,[1] V. A. Dolgikh,[1] E. S. Kuznetsova,[1] A. V. Olenev,[1,2] S. A. Klimin,[3] M. A. Kashchenko,[3,4] I. V. Budkin,[3,4] I. V. Yatsyk,[5,6] A. A. Demidov,[7] E. A. Zvereva,[1,8] and A. N. Vasiliev[1,8,9]

[1]*Moscow State University, 119991 Moscow, Russia*
[2]*Sine Theta Ltd., 119991 Moscow, Russia*
[3]*Institute of Spectroscopy, RAS, 142190 Troitsk, Russia*
[4]*Moscow Institute of Physics and Technology, 141707 Dolgoprudny, Russia*
[5]*Kazan Physical-Technical Institute, RAS, 420029 Kazan, Russia*
[6]*Kazan Federal University, 420008 Kazan, Russia*
[7]*Bryansk State Technical University, 241035 Bryansk, Russia*
[8]*National Research South Ural State University, 454080 Chelyabinsk, Russia*
[9]*National University of Science and Technology "MISiS," 119049 Moscow, Russia*

(Received 13 August 2017; revised manuscript received 27 September 2017; published 23 October 2017)

We present the synthesis and the experimental and theoretical study of the new member of the francisite family, $Cu_3Yb(SeO_3)_2O_2Cl$. The compound reaches an antiferromagnetic order at $T_N = 36.7$ K and experiences first-order spin-reorientation transition to weakly ferromagnetic phase at $T_R = 8.7$ K evidenced in specific heat C_p and magnetic susceptibility χ measurements. Distinctly different magnetization loops in $T < T_R$ and $T_R < T < T_N$ temperature ranges reflect the interplay of rare-earth and transition-metal subsystems. At low temperatures, the saturation magnetization $M_s \sim 5.2\,\mu_B$ is reached in pulsed magnetic-field measurements. The electron spin resonance data reveal the complicated character of the absorption line attributed to response from both copper and ytterbium ions. Critical broadening of the linewidth at the phase transitions points to quasi-two-dimensional character of the magnetic correlations. The spectroscopy of Yb^{3+} ions evidences splitting of the lowest-energy Kramers doublet of $^2F_{5/2}$ excited multiplet at $T_R < T < T_N$ while the ground Kramers doublet splits only at $T < T_R$. We describe the magnetic properties both above and below the spin-reorientation transition in the framework of a unified approach based on the mean-field approximation and crystal-field calculations.

DOI: 10.1103/PhysRevB.96.134422

I. INTRODUCTION

The francisite $Cu_3Bi(SeO_3)_2O_2Cl$ is characterized by a unique combination of chemical elements met in this mineral only [1]. Its crystal structure, however, is quite susceptible to various substitutions in both cation and anion sectors. Any of these substitutions may drastically change the francisite's physical properties [2–4]. In such way, the bromide $Cu_3Bi(SeO_3)_2O_2Br$ [5] misses a low-temperature structural phase transition seen in the chloride [6–10], while the as-prepared tellurite $Cu_3Bi(TeO_3)_2O_2Cl$ [11] realizes this low-temperature phase. Regarding magnetic properties, most important is the replacement of bismuth by rare earths.

The main feature of Bi francisite's layered crystal structure is the buckled kagome pattern of copper ions. This arrangement prevents the formation of long-range magnetic order for dominant antiferromagnetic interaction, but in the case of prevailing ferromagnetic interaction the kagome lattice may support the canted magnetic structure. The competition of ferromagnetic nearest-neighbor and antiferromagnetic next-nearest-neighbor exchange interactions is responsible for the formation of noncollinear magnetic structure in Bi francisite at $T_N = 24$ K, while weaker anisotropic terms fix the spin directions with respect to crystallographic axes [6]. The rare earth's anisotropy may influence this complex structure leading to temperature-driven spin-reorientation transition. Regarding magnetically active rare earths, which are not the cases of earlier studied Y [12], La [13], Eu, and Lu [14], the complex investigation of thermodynamic, resonance, and optical properties has been done for $Cu_3Sm(SeO_3)_2O_2Cl$ only. The second-order spin-reorientation transition in Sm francisite takes place at $T_R = 8.5$ K, while the Néel temperature shifts to $T_N = 35$ K [15].

Here, we present the results of thermodynamic properties, electron spin resonance, and infrared spectroscopy study of another member of this family, namely, the Yb francisite $Cu_3Yb(SeO_3)_2O_2Cl$. The treatment of thermodynamic data is provided within frames of mean-field theory and crystal-field (CF) calculations. In variance with Sm francisite, the spin reorientation in Yb francisite takes place as the first-order phase transition. In addition, the low-temperature magnetic properties of these two compounds were found to be distinctly different.

II. SYNTHESIS AND STRUCTURE REFINEMENT

$Cu_3Yb(SeO_3)_2O_2Cl$ has been synthesized from CuO (analytical grade; Ural Plant of Chemicals Reagents), $CuCl_2$ (99%; Merck), Yb_2O_3 (99+; Merck), and self-made SeO_2. Selenium dioxide was prepared by dehydration of selenous acid (99%; ChelChem) under vacuum of about 100 mTorr and temperature of about 80 °C. Dehydrated product was additionally purified by sublimation in a flow of anhydrous air and NO_2. Ytterbium oxide was additionally calcined in alumina crucible at 1100 °C for 48 h before using.

The stoichiometric mixture was loaded into a quartz tube in an argon-filled glow box in accordance with equation $5CuO + Yb_2O_3 + CuCl_2 + 4SeO_2 = 2Cu_3Yb(SeO_3)_2O_2Cl$.

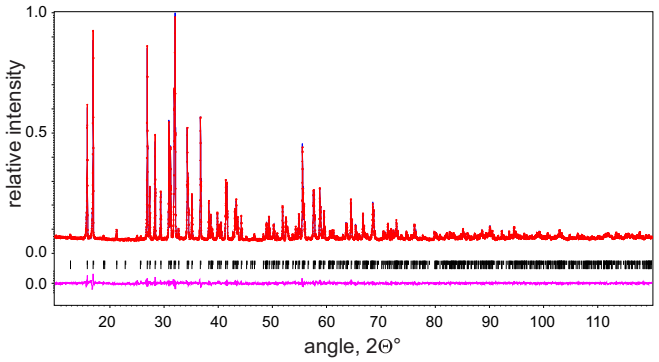

FIG. 1. The Rietveld plot for $Cu_3Yb(SeO_3)_2O_2Cl$ francisite.

The tube was sealed under pressure of about 50 mTorr and placed into the furnace. The sample treatment consists of heating within 12 h to 300 °C and keeping at 300 °C for 1 day. After that, the temperature was raised to 575 °C within 12 h and kept at this temperature for 3 days. Finally, the furnace was switched off and cooled down to room temperature. As a result, a green powder product was obtained. The single-phase nature of the product was confirmed by powder x-ray diffraction, the pattern being in accordance with that given in Ref. [16]. The x-ray diffraction measurements were carried out on a STOE STADI P diffractometer with germanium monochromator, Cu $K\alpha_1$ radiation, 2ϑ range $10°-85°$, equipped with an IP-PSD detector. The ICDD PDF-2 database was used as the reference.

Data collection for the structure refinement was performed on a STOE Theta/Theta setup employing Cu $K\alpha_1 + \alpha_2$ radiation at $T = 293$ K. The diffraction pattern was collected in 2ϑ range $10°-120°$ with 0.017° steps. The JANA2006 software [17] was used for the structure solution and refinement. The final Rietveld plot for $Cu_3Yb(SeO_3)_2O_2Cl$ is shown in Fig. 1. Crystallographic data are summarized in Table I. On

TABLE I. Crystallographic data and x-ray diffraction experiment details for $Cu_3Yb(SeO_3)_2O_2Cl$.

Composition	$Cu_3Yb(SeO_3)_2O_2Cl$
Space group	*Pmmn*
Instrument	STOE Theta/Theta
Radiation wavelength (Å)	Cu $K\alpha_1 + \alpha_2$
Unit cell parameters	
a (Å)	6.28278(3)
b (Å)	9.39486(5)
c (Å)	6.93291(3)
V (Å^3)	409.221(3)
Z	2
Temperature (K)	293
2θ range (deg)	10–120
Step (deg)	0.017
Number of points	6470
Parameters refined	62
R_p	0.0287
wR_p	0.0375
wR exp	0.0290
GOF	1.29
Method of background treatment	Six Legendre polynomials

TABLE II. Atomic coordinates and isotropic thermal parameters in $Cu_3Yb(SeO_3)_2O_2Cl$.

Atom	Position	x/a	y/b	z/c	U (Å^2)
Yb1	2*a*	1/4	1/4	0.26553(15)	0.0069(4)[a]
Cu1	4*c*	0	0	0	0.0185(8)[a]
Cu2	2*a*	1/4	1/4	0.7957(4)	0.0175(12)[a]
Se1	4*e*	1/4	0.56154(14)	0.59033(19)	0.0097(6)[a]
Cl1	2*b*	1/4	3/4	0.1417(6)	0.036(2)[a]
O1	4*e*	1/4	0.1128(8)	1.0055(10)	0.022(3)
O2	8*g*	0.0337(7)	0.5908(5)	0.7358(7)	0.0091(16)
O3	4*e*	1/4	0.1212(7)	0.571(1)	0.009(2)

[a]Equivalent parameter $U_{eq} = 1/3(U_{11} + U_{22} + U_{33})$.

the last steps of the refinement all atoms besides oxygen were fitted anisotropically. Atomic coordinates in the space group *Pmmn* (59) and equivalent isotropic thermal parameters are listed in Table II. Table III presents selected interatomic distances for $Cu_3Yb(SeO_3)_2O_2Cl$. According to data presented in Tables I–III the studied compound possesses francisitelike crystal structure, taking into account that ionic radius Yb^{3+} is smaller than that of Bi^{3+}. The Yb atom is situated in cubes formed by oxygen atoms (Table III). Two copper atoms are in square planar coordination by nearest oxygen atoms (Table III). Copper atoms in $Cu_3Yb(SeO_3)_2O_2Cl$ form a buckled kagome network. The Cu2-Cu1 distances within the net are 3.16 Å and Cu1-Cu1 are 3.14 Å. These values are shorter than those for $Cu_3Bi(SeO_3)_2O_2Cl$ reported in Ref. [2]. The morphology of the studied sample is that of a collection of irregular platelike grains with lateral dimensions ranging mostly in the range 1–10 μm. The importance of sample morphology is due to the fact that X-band electron spin resonance in francisites is quite sensitive to this factor.

III. MAGNETIZATION AND SPECIFIC HEAT

Thermodynamic properties of the pellets of $Cu_3Yb(SeO_3)_2O_2Cl$, i.e., specific heat C_p and magnetization M, in the temperature range $T = 2-300$ K under magnetic field B up to 9 T were studied using relevant options of the Quantum Design Physical Properties Measurement System

TABLE III. Selected interatomic distances in structure in $Cu_3Yb(SeO_3)_2O_2Cl$.

Bond	Multiplicity	d (Å)
Yb1-O2	4	2.327(5)
Yb1-O3	2	2.439(7)
Yb1-O1	2	2.216(7)
Cu1-Cl1	2	2.991(1)
Cu1-O2	2	2.032(5)
Cu1-O1	2	1.895(4)
Cu2-Cl1	2	3.171(1)
Cu2-O3	2	1.973(7)
Cu2-O1	2	1.943(7)
Se1-O3	1	1.722(7)
Se1-O2	2	1.714(5)

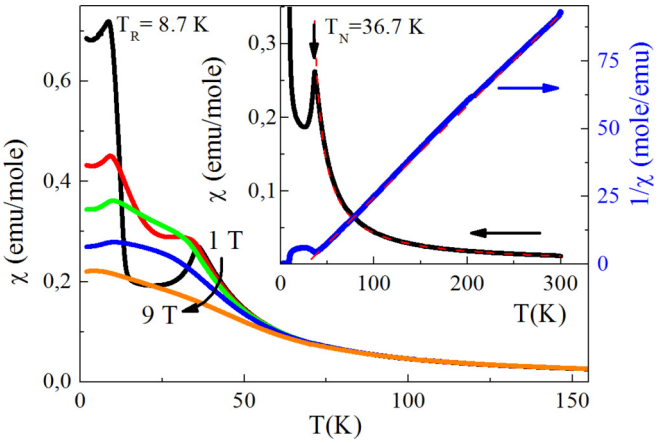

FIG. 2. The temperature dependencies of reduced magnetization $\chi = M/B$ in $Cu_3Yb(SeO_3)_2O_2Cl$ at various magnetic fields. The inset shows this dependence at $B = 1$ T and its reciprocal.

PPMS-9T. The pulsed magnetic-field measurements up to $B \sim 33$ T were provided by a homemade capacitance bank discharge setup. The temperature dependencies of magnetic susceptibility (or reduced magnetization) $\chi = M/B$ in Yb francisite taken at various magnetic fields are shown in Fig. 2. At elevated temperatures, the inverse magnetic susceptibility $\chi^{-1}(T)$ follows a straight line with cutoff at positive Weiss temperature $\Theta = 25$ K, which means the predominance of ferromagnetic exchange interactions.

The further analysis of $\chi(T)$ dependence in paramagnetic state and estimation of the effective magnetic moment in $Cu_3Yb(SeO_3)_2O_2Cl$ are hampered by the fact that both the Curie-Weiss term of Cu^{2+} ions and the Van Vleck term of Yb^{3+} ions contribute additively to the magnetic response of this compound. The sharp anomalies at $T_N = 36.7$ K and $T_R = 8.7$ K at cooling ($T_R = 9.0$ K at heating) are seen in low-field measurements. Both anomalies are rapidly suppressed by an external magnetic field. Similar to Sm francisite it is assumed that the magnetic ordering in Yb francisite takes place at T_N while the spin-reorientation transition occurs at T_R.

As shown in Fig. 3, the magnetization loops in $Cu_3Yb(SeO_3)_2O_2Cl$ experience remarkable evolution with temperature. At $T > T_N$, the $M(B)$ curves exhibit standard paramagnetic behavior. In the range $T_R < T < T_N$, the magnetization M increases linearly with magnetic field B until the critical value B_C where the first-order metamagnetic transition occurs. There are no residual magnetization and coercivity in this range. At lowest temperatures, $T < T_R$, the $M(B)$ curves evidence spontaneous magnetization with residual magnetization of 1.05 μ_B per formula unit and coercivity of about 0.2 T. The magnetization loops themselves are rather peculiar at $T < T_R$; while the onward curves exhibit ferromagnetic behavior, the downward curves are essentially linear at lowest temperatures. At low temperatures, the magnetization saturates at $M_s \sim 5.2\,\mu_B$, as shown in the inset to Fig. 3.

The temperature dependence of the specific heat C_p in $Cu_3Yb(SeO_3)_2O_2Cl$ is shown in Fig. 4. The λ-type anomaly at T_N denotes the second-order transition, while the sharp peak at T_R indicates the first-order transition. The suppression of the Néel transition by external magnetic field is illustrated by the

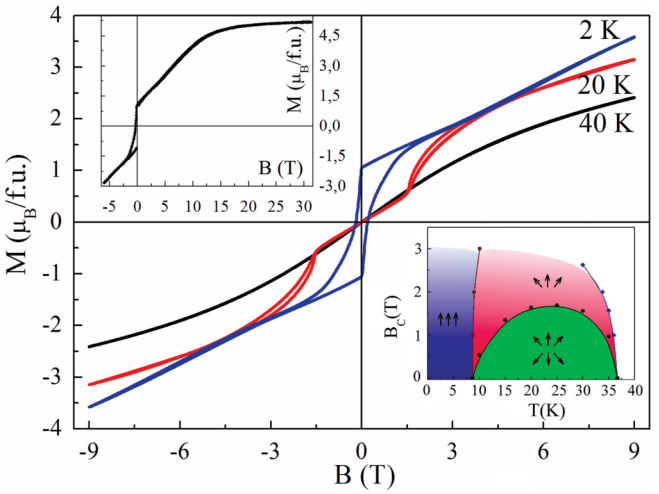

FIG. 3. The magnetization loops in $Cu_3Yb(SeO_3)_2O_2Cl$ at various temperatures. The upper inset represents the pulsed field magnetization at $T = 2.4$ K. The lower inset represents the schematic phase diagram.

upper inset in Fig. 4. Prior to suppression of the sharp peak at T_R by magnetic field, the Schottky-type anomaly develops in the vicinity of T_R. This anomaly is seen also above T_R when compared with the $C_p(T)$ curves obtained at both cooling and heating, as shown in the lower inset in Fig. 4.

IV. ELECTRON SPIN RESONANCE

The X-band electron spin resonance (ESR) study has been carried out using a Bruker EMX/plus spectrometer ($f = 9.4$ GHz) in the temperature range 5–110 K at $B \leqslant 1.4$ T. The typical ESR spectrum for a powder sample of $Cu_3Yb(SeO_3)_2O_2Cl$ in paramagnetic state is shown in the lower panel of Fig. 5. Similarly to reported results of ESR on various members of the francisite family [2,12–15], at elevated temperatures the spectra are presented by superposition of two resonance modes, i.e., broad L_1 and narrow L_2. The broad

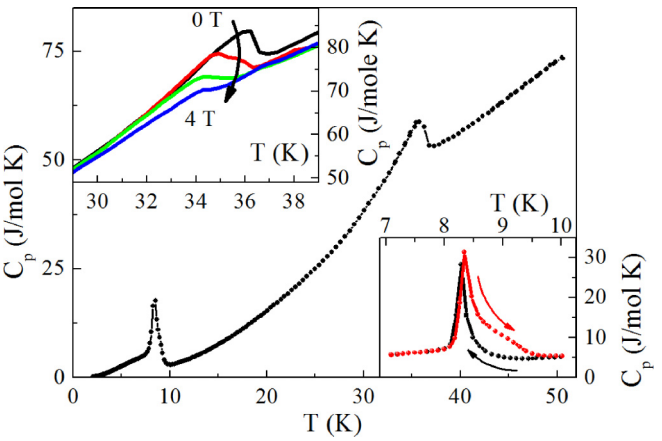

FIG. 4. The temperature dependence of specific heat C_p in $Cu_3Yb(SeO_3)_2O_2Cl$. The lower inset represents the hysteresis of singularity at T_R. The upper inset shows the magnetic field's evolution of singularity at T_N.

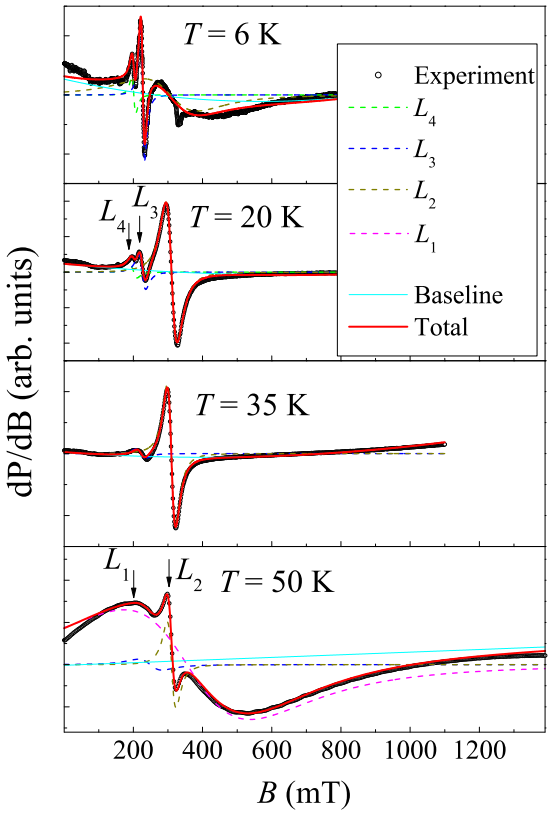

FIG. 5. The ESR spectra for $Cu_3Yb(SeO_3)_2O_2Cl$ at various temperatures. The circles are experimental data, the dashed lines are resolved components, and the solid lines are their summation.

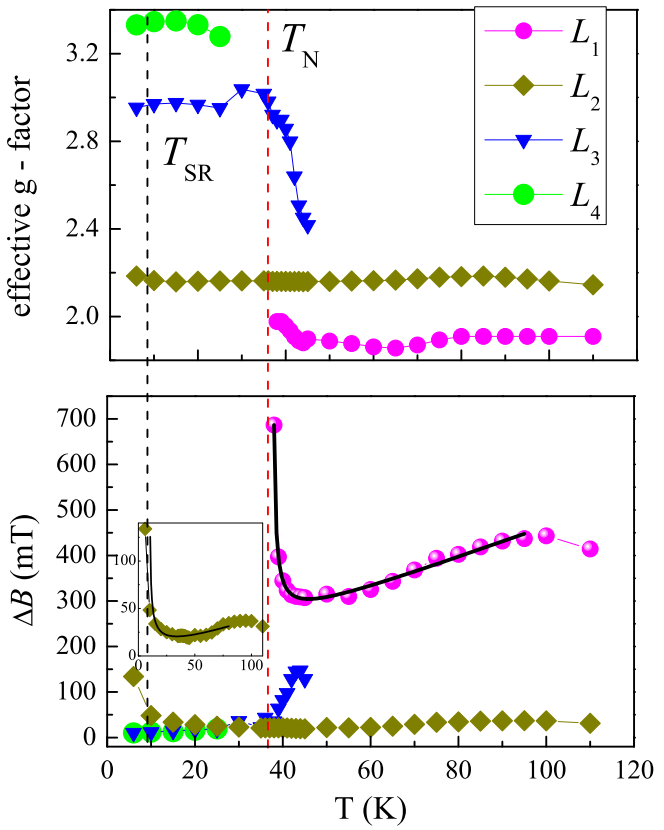

FIG. 6. The temperature dependencies of the effective g factors and the linewidths for resolved components of ESR spectra. Inset: enlarged scale for the $\Delta B_2(T)$ dependence.

line L_1 abruptly vanishes at the onset of long-range order at T_N. The narrow line L_2 persists down to low temperature being virtually insensitive to magnetic ordering. Tentatively, the broad line L_1 reflects the response of Cu^{2+} ions within the bulk of the sample being shifted with respect to the narrow line L_2 due to the presence of an internal magnetic field well above the Néel temperature. The narrow line L_2 reflects the response of a small percentage of Cu^{2+} ions at the surface of crystal grains being essentially nonsensitive to this field.

There is one more absorption line L_3 which becomes clearly visible at $T < T_N$, as shown in the upper panels in Fig. 5. This line with an effective g factor of about 3, can be attributed to Yb^{3+} ions [18]. At lowest temperatures the shape of the L_3 mode is anisotropic and the signal splits into two distinct peaks, L_3 and L_4, ascribed to parallel and perpendicular components of the g tensor of Yb^{3+} ions.

To draw conclusions about the spin dynamics of $Cu_3Yb(SeO_3)_2O_2Cl$ and to obtain the evolution of the corresponding ESR parameters with temperature we analyzed the ESR line shape. It was found that in different temperature ranges the experimental line can be properly described by the sum of two or three components taken in Lorentzian form. Since the absorption line is relatively broad at high temperature (the same order as the resonance field), two circular components of the exciting linearly polarized microwave field have to be taken into account.

The results of the ESR line shape fitting are shown by the solid lines in Fig. 5. Apparently, the fitted curves are in good agreement with the experimental data. Representative examples of the spectrum decomposition along with several resolved resonance modes are given at various temperatures to highlight the spectrum evolution and consequent appearance/disappearance of the corresponding modes. The temperature dependencies of the effective g factor and the linewidths ΔB for the resolved resonance modes are shown in Fig. 6. The average values of effective g factor are estimated as $g_1 = 1.7 \pm 0.3, g_2 = 2.17 \pm 0.05, g_3 = 2.95 \pm 0.10$, and $g_4 = 3.35 \pm 0.10$ (upper panel). The g value for the L_1 line is affected by an internal magnetic field while the g value for the L_2 line is consistent with the typical values of g factor of Cu^{2+} ions [19,20].

Both ΔB_1 and ΔB_2 linewidths related to the copper subsystem demonstrate nonmonotonic behavior indicating different spin-dynamic regimes over the temperature range studied (lower panel in Fig. 6). Remarkably, the changes in temperature dependence of the linewidth occur in a similar manner for both these modes, confirming the common origin of L_1 and L_2. At cooling, the linewidths decrease weakly and pass through a minimum above T_N for the L_1 mode and T_R for the L_2 mode. Upon further decrease of the temperature the absorption line broadens significantly and the ESR signal degrades in the vicinity of T_N for the L_1 mode and T_R for the L_2 mode. The linewidths of the L_3 and L_4 modes assigned to the ytterbium subsystem are almost temperature independent.

TABLE IV. The main parameters of ESR spectra in $Cu_3Yb(SeO_3)_2O_2Cl$.

Line	ΔB_0 (mT)	A (mT)	T_{crit} (K)	β	C (mT/K)
L_1	109 ± 10	10 ± 2	37 ± 1	0.8 ± 0.2	3.5 ± 0.2
L_2	14 ± 1	31 ± 1	8.7 ± 1	0.5 ± 0.2	0.4 ± 0.1

The broadening of the ESR line may be treated in terms of critical behavior of ESR linewidth due to slowing down of spin fluctuations in the vicinity of an order-disorder transition [21–23]. This causes the divergence of the spin correlation length, which in turn affects the spin-spin relaxation time of exchange-narrowed ESR lines. To account for the ΔB behavior over the whole temperature range we used the modified formula suggested for two-dimensional (2D) magnets [24] which includes additionally the linear term $\Delta B(T) = \Delta B_0 + A[T_{crit}/(T - T_{crit})]^{\beta} + CT$. Here, the first term ΔB_0 describes the limiting temperature-independent linewidth for the exchange-narrowed regime, while the second term reflects the critical behavior with T_{crit} being the temperature of the magnetic transition and β the critical exponent. Solid lines on the lower panel and in the inset to Fig. 6 represent the least-square fit of the $\Delta B_1(T)$ and $\Delta B_2(T)$ experimental data. The best fit has been obtained with the parameters summarized in Table IV.

In the framework of Kawasaki's approach [21], the absolute value of the critical exponent can be expressed as $\beta = [(7 + \eta)\nu/2 - 2(1 - \zeta)]$, where ν describes the divergence of correlation length, η is a critical exponent for the divergence of static correlations, and ζ reflects the divergence of the specific heat. Using the values $\eta = \zeta = 0$ and $\nu = 2/3$ for three-dimensional Heisenberg antiferromagnets [21], β should take a value of $1/3$. In the case of low-dimensional magnets, the critical exponent is expressed as $\beta = (3 - 2\eta)\nu$ and $(3.5 - 2\eta)\nu$ for 2D and 1D systems, respectively [25,26]. The corresponding values β using the values $\eta = 0$ and $\nu = 1/2$ [16] result in $\beta = 3/2$ and $7/4$ for 2D and 1D systems, respectively. So, one can conclude that the enhanced values of the critical exponents β_i listed in Table IV support the scenario of quasi-two-dimensional character of magnetic correlations in $Cu_3Yb(SeO_3)_2O_2Cl$.

V. INFRARED SPECTROSCOPY

With the aim to get additional information about the nature of phase transitions in $Cu_3Yb(SeO_3)_2O_2Cl$ we investigated the infrared transmission spectra in the range of CF transitions in Yb^{3+} ions. The energy levels of Kramers rare earths are degenerated and can be split by a magnetic field of any origin including an effective magnetic field arising in a magnetically ordered phase [27–29]. The Yb^{3+} ion has an odd number of electrons in $4f^{13}$ electronic configuration with one hole in the $4f$ shell, and the simplest energy scheme of electronic levels among the lanthanide series with two multiplets, i.e., ground $^2F_{7/2}$ and excited $^2F_{5/2}$, as shown in Fig. 7(a). In the crystal structure of francisite, the ytterbium ions occupy the sites with C_{2v} symmetry. The crystal field splits multiplets into $(2J + 1)/2$ Kramers doublet (J is the total moment of the Yb^{3+} ion).

For optical spectroscopy measurements, the sample of $Cu_3Yb(SeO_3)_2O_2Cl$ was ground in agate mortar, mixed with an optical-grade KBr, and pressed into a pellet, which was put into the optical closed-cycle cryostat Cryomech PT-403. The transmission spectroscopy experiment was performed with the aid of a Bruker IFS125HR Fourier-transform spectrometer in the spectral range $9000-12000\,cm^{-1}$, and the temperature was varied from 4 to 300 K.

The infrared transmission spectra of $Cu_3Yb(SeO_3)_2O_2Cl$ taken at various temperatures are shown in Fig. 7(b). The spectra contain narrow absorption lines due to *f-f* transitions in Yb^{3+} ions. The most intense is the IA line at $10\,330\,cm^{-1}$ corresponding to the transition from level I of ground multiplet $^2F_{7/2}$ to the first level A of excited multiplet $^2F_{5/2}$. There are also weaker lines in the spectra. The line at $10\,225\,cm^{-1}$ is identified as the IIA transition. Its intensity decreases rapidly at cooling due to depletion of the level II. Thus, the first excited

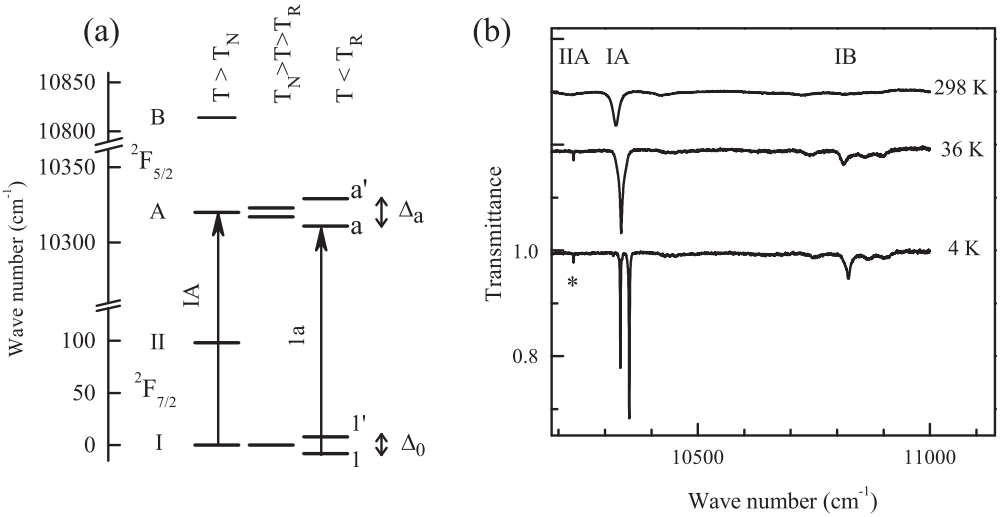

FIG. 7. The scheme of level splitting in Yb^{3+} ions at various temperature ranges (a). The infrared transmission spectra in $Cu_3Yb(SeO_3)_2O_2Cl$ at several temperatures (b).

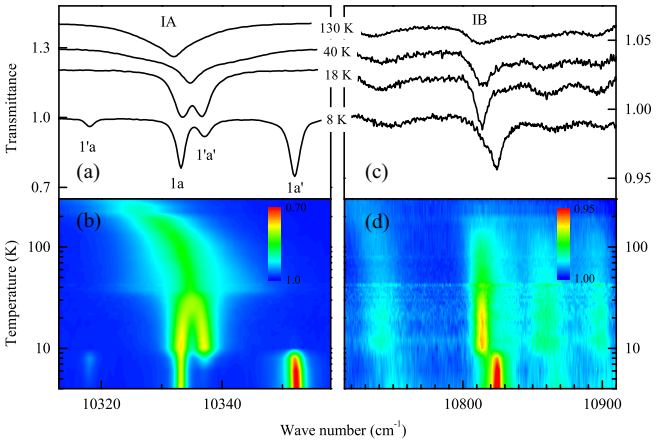

FIG. 8. The infrared transmission spectra of $Cu_3Yb(SeO_3)_2O_2Cl$ at several temperatures in the spectral region of IA (a) and IB (b) transitions and corresponding color maps (b),(d).

Kramers doublet is separated by the energy 105 cm^{-1} from the ground doublet. The line at 10 823 cm^{-1} is attributed to the IB transition. The rest of the lines can be attributed to vibronic transitions or missing transition IC.

Figures 8(a)–8(d) present detailed temperature dependencies in the spectral regions of the IA and IB transitions. At cooling, the lines shift and narrow. At T_N, the IA line splits into two components. This is due to splitting of either one or two Kramers doublets corresponding to initial and final states. The splitting evidences the appearance of the internal magnetic field due to magnetic ordering. Note that the line IIA does not split experiencing only slight narrowing. This means that the ground Kramers doublet, marked as I on the scheme [Fig. 7(a)], does not split in the temperature range $T_R < T < T_N$. At further lowering of temperature, in the vicinity of T_R the spectra changes abruptly for both IA and IB transitions. In the former case, four components appear which results from the change in the Kramers doublets splitting of both initial and final states. The level scheme for the magnetic phase at $T < T_R$ is given in Fig. 7(a). In the latter case, the IB line experiences a sharp shift that confirms the splitting of the ground Kramers doublet. Therefore, two magnetic phase transitions are fixed by infrared spectroscopy in $Cu_3Yb(SeO_3)_2O_2Cl$.

Spontaneous magnetic ordering leads to the appearance of an effective magnetic field $\boldsymbol{B}_{\text{eff}}$ acting on the rare-earth ion by the ordered copper subsystem. One has to take into account the anisotropic magnetic properties of the rare-earth ion arising from CF effects. The splitting of the kth CF level in a frame of mean-field theory can be considered as the Zeeman effect in an effective magnetic field:

$$\Delta_k = \sqrt{\sum_i \left(g_{ki} B_{\text{eff}}^{ki}\right)^2},$$

where $i = x, y, z, g_{ki}$ and B_{eff}^{ki} are ith components of the magnetic g factors of the rare-earth ion and the effective magnetic field. The absence of the splitting of the ground Kramers doublet of a Yb^{3+} ion in the range $T_R < T < T_N$ can be explained by the fact that $\boldsymbol{B}_{\text{eff}}$ is directed in such a way that the corresponding component of the ytterbium g factor is close to zero. An abrupt change of splitting at T_R points to the rotation of $\boldsymbol{B}_{\text{eff}}$ due to the spin-reorientation process. Although the copper magnetic subsystem is turned to the state with higher energy, the ytterbium ground state is lowered so that the system gains in energy.

While the high-temperature phase transition at T_N takes place as a second-order one, which is evidenced by the gradual change of the splitting of line IA, the low-temperature one at T_R is a first-order phase transition, as the spectrum is changed abruptly. To study the low-temperature phase transition in more detail we have measured transmission spectra with small temperature steps around T_R while heating and cooling the sample. The results are shown in Fig. 9. The first conclusion is that in the small temperature range (less than 2 K) around T_R two phases coexist. According to a theory of spin-reorientation phase transitions [30], the coexistence of two phases is an intrinsic property of a first-order spin-reorientation phase transition. We can use an intensity of line IA (10 353 cm^{-1}), shown in Figs. 8(a) and 9(a), as a quantitative estimation of the amount of low-temperature phase in a crystal. The dependence

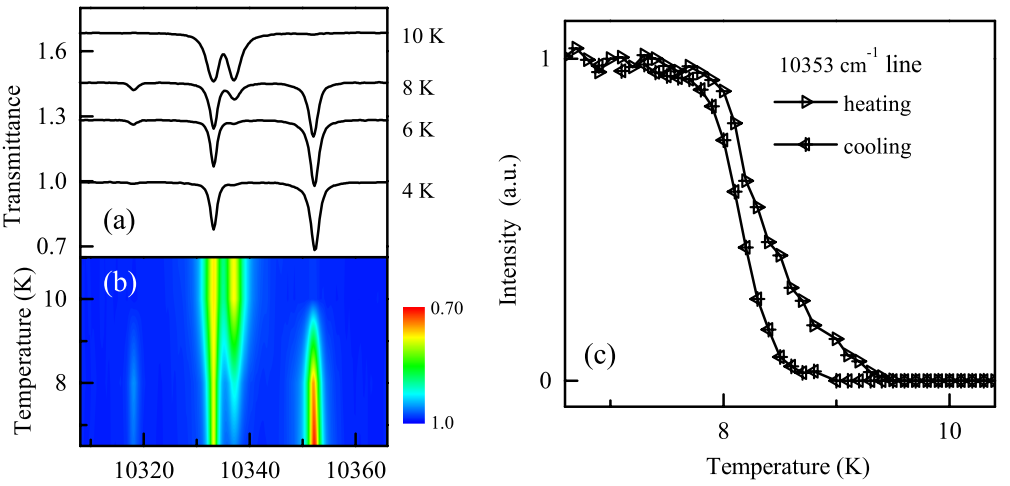

FIG. 9. The temperature evolution of infrared spectra of $Cu_3Yb(SeO_3)_2O_2Cl$ in the vicinity of T_R as transmission spectra (a) and color map (b). The intensity of the spectral line at 10 353 cm^{-1} as the function of temperature (c).

obtained demonstrates hysteresis in coincidence with the heat capacity data presented above, which is also an intrinsic property of first-order spin-reorientation transitions [30].

A comparison of the data obtained in this work on $Cu_3Yb(SeO_3)_2O_2Cl$ with that of samarium francisite $Cu_3Sm(SeO_3)_2O_2Cl$ [15] shows that in both compounds spin-reorientation transition arises due to the strong rare-earth single-ion anisotropy. However, different scenarios for this phase transition are realized. In $Cu_3Sm(SeO_3)_2O_2Cl$, the spin-reorientation transition is of second order, while in $Cu_3Yb(SeO_3)_2O_2Cl$ it is of first order.

We presume that the reason for that lies in the magnetic properties of rare-earth ions, namely, in different single-ion anisotropies of samarium and ytterbium. The rare earths, unlike the *d* ions, possess a strong magnetic anisotropy due to the crystal-field effects. For example, the study of the family of rare-earth nickelates R_2BaNiO_5 [29] with orthorhombic structure and C_{2v} symmetry for rare-earth sites (similar to francisites) have revealed different types of single-ion anisotropies for different rare earths with three main types of ground-state magnetic *g* factor $(g_x,0,0)$, $(0,g_y,0)$, and $(0,0,g_z)$. This situation could be also realized in the family of rare-earth francisites. Taking into account the data of neutron studies of the magnetic structure of $Cu_3Bi(SeO_3)_2O_2Cl$ [5] one can conclude that after the ordering of the copper subsystem at T_N the mean field $\boldsymbol{B}_{\text{eff}}$ acting on rare-earth ions in the francisite structure is directed along the *z* axis. This direction coincides with the twofold axis of the C_{2v} site of the rare-earth ion. The absence of the splitting of ground Kramers doublets for both samarium and ytterbium ions in corresponding francisite compounds means that they possess *XY*-like anisotropy. In this case two main possibilities exist, namely, when the maximal component of the *g* factor is g_x or g_y. During spin-reorientation transition $\boldsymbol{B}_{\text{eff}}$ have to rotate from the *z* axis to the *x* axis in one case and to the *y* axis in another one to explain the experimental data on the splitting of ground Kramers doublet. Depending on anisotropic interactions in a crystal, in one case the spin-reorientation transition can be realized as spin-flop-like (first order) or as gradual rotation (second order). Thus, different anisotropies of samarium and ytterbium can explain different scenarios of low-temperature magnetic transition.

VI. CALCULATIONS

The magnetic properties of $Cu_3Yb(SeO_3)_2O_2Cl$ are determined by both rare-earth and copper subsystems interacting with each other. The copper subsystem is organized by two antiferromagnetic sublattices, where both types of copper, i.e., two Cu1 ions ($\mathbf{M}_i^{2\text{Cu1}}$) and one Cu2 ion ($\mathbf{M}_i^{\text{Cu2}}$), contribute to the sublattice's magnetization $\mathbf{M}_i^{\text{Cu}}$. The rare-earth subsystem magnetized through *f-d* interaction is constituted by two antiferromagnetic sublattices also. In present calculations we used the approach developed for description of particular *f-d* compounds, i.e., rare-earth ferroborates [31–33]. This approach is based on the CF model for the rare-earth ion within mean-field approximation. In accordance with the magnetic structure and hierarchy of exchange interactions in Yb francisite, the effective Hamiltonians for Yb^{3+} ions in the *i*th sublattice ($i = 1,2$) under magnetic field $\mathbf{B}$ can be written

$$\mathcal{H}_i(Yb) = \mathcal{H}_i^{\text{CF}} - g_J\mu_B\mathbf{J}_i\left[\mathbf{B} + \lambda_{fd1}\mathbf{M}_i^{2\text{Cu1}} + \lambda_{fd2}\mathbf{M}_i^{\text{Cu2}}\right], \tag{1}$$

where $\mathcal{H}_i^{\text{CF}}$ is the CF Hamiltonian, g_J is the Landé factor, $\mathbf{J}_i$ is the operator of angular moment of the Yb^{3+} ion, and $\lambda_{fd1,2} > 0$ are the molecular constants of the Yb-Cu1,2 interaction.

The magnetic moments of copper $\mathbf{M}_i^{\text{Cu1,2}}$ and rare-earth $\mathbf{m}_i^{\text{Yb}}$ ions are

$$\mathbf{M}_i^{\text{Cu1,2}} = g_S\mu_B\langle\mathbf{S}_i^{\text{Cu}}\rangle, \quad \mathbf{m}_i^{\text{Yb}} = g_J\mu_B\langle\mathbf{J}_i\rangle, \tag{2}$$

where $g_S = 2.17$ is the *g* value and $\mathbf{S}_i^{\text{Cu}} = 1/2$ is the operator of spin moment.

The molecular constants $\lambda_{fd1,2}$ in Eq. (1) are related to the parameters $J_{fd1,2}$ in the Hamiltonian $\mathcal{H}_{fd1,2} = J_{fd1,2}\mathbf{S}^{\text{Yb}}\mathbf{S}^{\text{Cu}}$ by expressions $\lambda_{fd1,2} = \frac{1}{g_J\mu_B}\frac{(g_J-1)}{g_S\mu_B}J_{fd1,2}$, obtained through relation $\mathbf{S}^{\text{Yb}} = (g_J - 1)\mathbf{J}$ and expression for $\mathbf{M}_i^{\text{Cu1,2}}$.

When calculating the magnetic properties of $Cu_3Yb(SeO_3)_2O_2Cl$, the possibility of the magnetic ordering within the rare-earth subsystem itself was considered also and the Hamiltonian of the exchange interaction $\mathcal{H}_i^{ff} = \lambda_{ff}\mathbf{m}_j^{\text{Yb}}\mathbf{J}_i$ was added to the Hamiltonian (1). However, the comparison with experimental data reveals no importance of the *f-f* exchange. Therefore, in the final form of the Hamiltonian (1) the Hamiltonian $\mathcal{H}_i^{ff}$ is omitted.

The CF Hamiltonian $\mathcal{H}^{\text{CF}}$ can be written in terms of irreducible tensor operators $C_q^{(k)}$:

$$\begin{aligned}\mathcal{H}^{\text{CF}} = {} & B_0^2C_0^{(2)} + B_2^2\left(C_2^{(2)} + C_{-2}^{(2)}\right) + B_0^4C_0^4 + B_2^4\left(C_2^{(4)} + C_{-2}^{(4)}\right) \\ & + B_4^4\left(C_4^{(4)} + C_{-4}^{(4)}\right) + B_0^6C_0^{(6)} + B_2^{(6)}\left(C_2^{(6)} + C_{-2}^{(6)}\right) \\ & + B_4^6\left(C_4^{(6)} + C_{-4}^{(6)}\right) + B_6^6\left(C_6^{(6)} + C_{-6}^{(6)}\right).\end{aligned} \tag{3}$$

Here, the B_q^k are the CF parameters for the orthorhombic symmetry.

No CF parameters B_q^k are known for Yb^{3+} ions in $Cu_3Yb(SeO_3)_2O_2Cl$. Moreover, there is no information on the parameters B_q^k for any other rare-earth francisite. Also no CF parameters are known for Yb^{3+} ions which occupy the site with C_{2v} symmetry in any other compounds of orthorhombic symmetry.

To describe the low-temperature thermodynamic properties of rare-earth compounds we have to consider the ground multiplet only. According to infrared spectroscopy data, the first excited doublet of the Yb^{3+} ion is at considerable distance ($\Delta \approx 105\,\text{cm}^{-1}$) from the ground doublet [see Fig. 7(a)]. Thus, to describe the low-temperature magnetic properties it is sufficient to take into account the ground doublet only. This allows not using in calculations the exact values of the CF parameters for Yb^{3+} ions.

In order to determine the CF parameters B_q^k we have used the experimental data of the magnetic susceptibility $\chi(T)$ and magnetization curves $M(B)$ in the paramagnetic state ($T > T_N$), data of heat capacity $C_p/T(T)$, and infrared spectroscopy of $Cu_3Yb(SeO_3)_2O_2Cl$. As initial CF parameters, from which the procedure of minimization of the corresponding target function was started, the parameters for the Er^{3+} ion in an orthorhombic crystal Er_2BaNiO_5 have been used [34]. The

Er^{3+} ion is close to the Yb^{3+} ion in the rare-earth series and occupies the site with C_{2v} symmetry in Er_2BaNiO_5 [34], as well as the Yb^{3+} ion in $Cu_3Yb(SeO_3)_2O_2Cl$. As a result, using the listed criteria we chose the following set that provides the best description of the experimental data (B_q^k, in cm^{-1}):

$$B_0^2 = 333, \quad B_2^2 = 696, \quad B_0^4 = 988,$$
$$B_2^4 = -695, \quad B_4^4 = -1199, \quad B_0^6 = 12,$$
$$B_2^6 = 994, \quad B_4^6 = 48, \quad B_6^6 = -927. \tag{4}$$

This approach allows calculating the magnetization, susceptibility, and rare-earth contribution to the heat capacity in Yb francisite. Since the CF parameters (4) were determined using the experimental data on the powder sample, they should be considered preliminary and the obtained results of calculations should be considered as the qualitative ones. The experimental data on magnetic properties measured along the main crystallographic axes, could be used to refine the B_q^k parameters. However, no successful attempts to grow the single crystals of rare-earth francisites were reported.

The magnetization and magnetic susceptibility of $Cu_3Yb(SeO_3)_2O_2Cl$ are

$$\mathbf{M} = \frac{1}{2}\sum_{i=1}^{2}\left(\mathbf{M}_i^{\mathrm{Cu}} + \mathbf{m}_i^{\mathrm{Yb}}\right), \quad \chi_k = \chi_k^{\mathrm{Cu}} + \chi_k^{\mathrm{Yb}}, \quad k = a,b,c. \tag{5}$$

To compare the results of calculations with experimental data obtained on the powder sample, we presumed averaging of magnetization and magnetic susceptibility along main the crystallographic axes:

$$M = \tfrac{1}{3}(M_a + M_b + M_c), \quad \chi = \tfrac{1}{3}(\chi_a + \chi_b + \chi_c). \tag{6}$$

To compute the value and orientation of the magnetic moment of Yb subsystem $\mathbf{m}_i^{\mathrm{Yb}}$ the self-consistent problem has to be solved on the basis of Hamiltonian (1) taking into account the Yb-Cu interactions in the ordered phase.

The magnetic moment of the Cu subsystem $\mathbf{M}_i^{\mathrm{Cu}} = \mathbf{M}_i^{2\mathrm{Cu1}} + \mathbf{M}_i^{\mathrm{Cu2}}$ was found by calculating the moment projections $\mathbf{M}_i^{\mathrm{Cu1}}$ and $\mathbf{M}_i^{\mathrm{Cu2}}$ to the external field $\boldsymbol{B}$. These projections are described by the field dependencies of the polar θ_i(B) and azimuth $\varphi_i(B)$ angles of the moments $\mathbf{M}_i^{\mathrm{Cu1}}$ and $\mathbf{M}_i^{\mathrm{Cu2}}$. The initial data on the $\theta_i(B)$ and $\varphi_i(B)$ dependencies were taken as measured along different crystallographic axes in $Cu_3Bi(SeO_3)_2O_2Br$ single crystal [5].

At $T < T_N$, the low-field magnetic susceptibility of Yb francisite can be determined using initial linear parts of the magnetization curves calculated for various directions of the external field. In paramagnetic phase, the magnetic susceptibility of a rare-earth subsystem can be estimated using Van Vleck's formula for the energy spectrum and wave functions calculated on the basis of the CF Hamiltonian (1). For the Cu subsystem, the susceptibility can be described in terms of the Curie-Weiss law.

The contribution of the Yb subsystem to the magnetic heat capacity of $Cu_3Yb(SeO_3)_2O_2Cl$ was calculated using formula

$$C^{\mathrm{Yb}} = k_B \frac{\langle E^2\rangle - \langle E\rangle^2}{(k_B T)^2}. \tag{7}$$

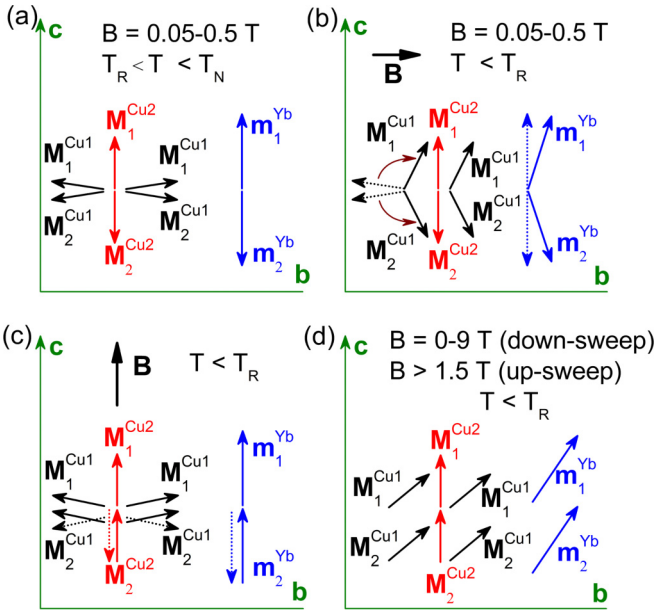

FIG. 10. The schemes of orientations of the magnetic moments within copper $\mathbf{M}_i^{\mathrm{Cu1,2}}$ and rare-earth $\mathbf{m}_i^{\mathrm{Yb}}$ sublattices used in the calculation of the magnetic parameters of $Cu_3Yb(SeO_3)_2O_2Cl$ (the axis a is oriented perpendicular to the plane).

The thermal averages $\langle E^2\rangle$ and $\langle E\rangle^2$ were calculated for the spectrum of the Yb^{3+} ion formed by the CF and by interactions with the Cu subsystem.

VII. DISCUSSION

To calculate the magnetic properties of Yb francisite in a magnetic field directed either along or perpendicular to the c axis, we used the schemes of orientation of the magnetic moments of copper $\mathbf{M}_i^{\mathrm{Cu1,2}}$ and rare-earth $\mathbf{m}_i^{\mathrm{Yb}}$ ions, as shown in Fig. 10. The calculation of magnetization $M_{a,b,c}(B)$ of the Yb subsystem (at $T = 2$ K) with the CF parameters (4) results in magnetization saturation $M_s^{\mathrm{Yb}} \approx 1.72\,\mu_B$ which is two times less than the net value of the Yb^{3+} moment. The CF of orthorhombic symmetry does not allow the Yb^{3+} ion to be magnetized to its maximal value, which is in correspondence with the measured saturation value $M_s \sim 5.2\,\mu_B$ in $Cu_3Yb(SeO_3)_2O_2Cl$ at 2 K (cf. upper inset to Fig. 3). The variation in the parameters B_q^k within reasonable limits does not lead to a significant change in the saturation value M_s.

In order to describe the temperature and field dependencies of magnetization the various mutual orientations of Yb^{3+} and Cu^{2+} magnetic moments are to be considered. It was found that no fully compensated schemes of the magnetic moment orientations allow describing the experimentally observed value of magnetic susceptibility χ at $T < T_R$. To describe $\chi(T)$ data in this temperature range, the reorientation of the Cu moments is needed. It was found also that the magnetic properties of Yb francisite could be described only if Yb-Cu1,2 exchange is different for Cu1 and Cu2 ions. Namely, the Yb-Cu2 exchange ($J_{fd2}^{c,ab}$) is to be substantially smaller than the Yb-Cu1 exchange ($J_{fd1}^{c,ab}$), i.e., $J_{fd1}^{c,ab} = 89$ K and $J_{fd2}^{c,ab} = 2.2$ K.

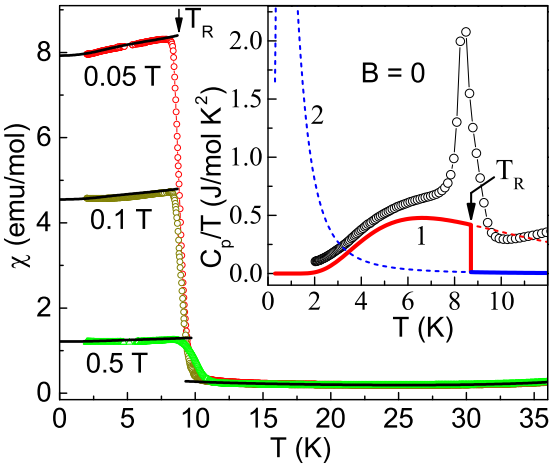

FIG. 11. The calculated (lines) and experimental (symbols) temperature dependencies of reduced magnetization $\chi = M/B$ in $Cu_3Yb(SeO_3)_2O_2Cl$ at various magnetic fields. The inset shows calculated and experimental temperature dependencies of specific heat $C_p/T(T)$ in $Cu_3Yb(SeO_3)_2O_2Cl$ at $B = 0$. Curve 1 represents the results of calculation for the scheme shown in Fig. 10(b); curve 2 corresponds to the scheme shown in Fig. 10(a).

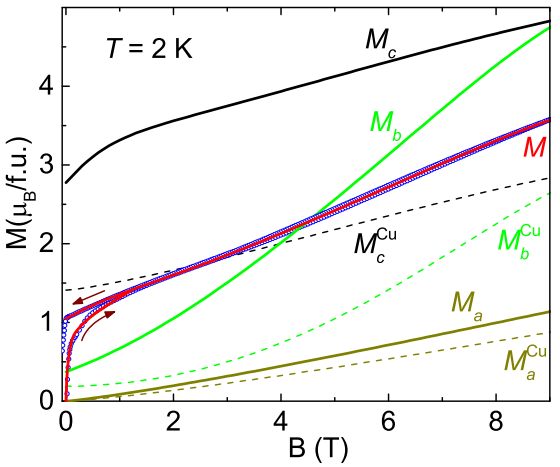

FIG. 12. The calculated (lines) and experimental (symbols) magnetization curves at $T = 2$ K. The resulting calculated curve $M(B)$ and its components $M_{a,b,c}(B)$ (for down sweep of the magnetic field) are shown. Calculated contributions of the Cu subsystem $\mathbf{M}^{Cu}_{a,b,c}$(B) to the total magnetization are shown by dashed curves.

As can be seen from Fig. 10(a), in the range $T_R < T < T_N$ the antiparallel orientations of the $\mathbf{M}_i^{Cu1}$ moments within each of two antiferromagnetic sublattices compensate each other. Thus, the total moment of the Cu subsystem in one sublattice ($\mathbf{M}_i^{Cu} = \mathbf{M}_i^{2Cu1} + \mathbf{M}_i^{Cu2}$) is defined by the $\mathbf{M}_i^{Cu2}$ moment. The *f-d* exchange in this case is weakened and the splitting of the ground doublet Δ_0 of the Yb^{3+} ion is minimal. According to the infrared spectroscopy data, the splitting Δ_0 at $T_R < T < T_N$ tends to zero. In the case of isotropic *f-d* exchange, the calculated splitting is $\Delta_0 \approx 1.37\,cm^{-1}$ for $\theta^{Cu1} = 85°$ being the angle between $\mathbf{M}_1^{Cu1}$ moments and the *c* axis [cf. Fig. 10(a)]. For the angle $\theta^{Cu1} = 90°$ the splitting is $\Delta_0 \approx 0.36\,cm^{-1}$. If the Yb-Cu2 exchange is neglected ($J^{c,ab}_{fd2} = 2.2$ K) the splitting is $\Delta_0 \approx 1\,cm^{-1}$ at $\theta^{Cu1} = 85°$ and $\Delta_0 = 0$ at $\theta^{Cu1} = 90°$. Note that in the case of the anisotropic *f-d* exchange ($J^c_{fd1,2} < J^{ab}_{fd1,2}$) the splitting Δ_0 tends to zero for the smaller angle θ^{Cu1}, i.e., at $J^c_{fd1,2} = 0.2\ J^{ab}_{fd1,2}$ the angle $\theta^{Cu1} = 75°$. Upon the reorientation of the $\mathbf{M}_i^{Cu1}$ moments along the *b* axis [cf. Fig. 10(b)], the total moment of the Cu subsystem in each sublattice increases sharply, which leads to a sharp increase in the value of splitting $\Delta_0 \approx 15\,cm^{-1}$ (at the angle $\theta^{Cu1} = 28.4°$) at $T < T_R$. As shown in Fig. 11, the quality of fitting of the experimental curves $\chi(T)$ in a magnetically ordered state is quite good using the schemes shown in Figs. 10(a) and 10(b).

The calculated magnetization curve $M(B)$ at $T = 2$ K for up and down sweeps of the magnetic field and the field dependencies of the components $M_{a,b,c}(B)$ for down sweep are shown in Fig. 12. Evidently, within the mean-field approach the experimental magnetization curves can be fitted as well. The curve $M(B)$ for the up-sweep field in the range $B = 0 - 1.5$ T was calculated as follows. At $B = 0$, the residual magnetization is absent in accordance with the scheme shown in Fig. 10(a). Then, as the field increases, the unfavorably directed moments of the Cu subsystem reorient along both the *c* axis [cf. Fig. 10(c)] and the *b* axis. As a result, at $B > 1.5$ T the state shown in Fig. 10(d) is realized. For the down sweep of the magnetic field, the total magnetization in the range $B = 0 - 9$ T is also well described by the scheme shown in Fig. 10(d).

Figure 12 shows also the calculated contributions of Cu subsystem $\mathbf{M}^{Cu}_{a,b,c}(B)$ (dashed curves) to the total magnetization of the Yb francisite for the down-sweep field. The character of the dependence on the field of the curves $\mathbf{M}^{Cu}_{a,b,c}(B)$ agrees basically with experimentally found magnetization curves in the rare-earth-free francisites $Cu_3Bi(SeO_3)_2O_2Cl$ [10] and $Cu_3Bi(SeO_3)_2O_2Br$ [5].

The calculations showed that the description of the low-field linear part of the $M(B)$ curve at $T > T_R$ (Fig. 3) needs an antiparallel orientation of the magnetic moments along the easy-axis direction. It is found that the calculation of the magnetization according to the scheme shown in Fig. 10(a) with antiparallel orientation of the Cu2 moments describes well the low-field linear part of the curve $M(B)$ at $T = 20$ K. Then, as the field is increased, the state shown in Fig. 10(d) is realized.

The inset to Fig. 11 represents the experimental data for the specific heat in $Cu_3Yb(SeO_3)_2O_2Cl$ as C_p/T vs T dependence. In this representation, the Schottky anomaly at about 6 K is clearly seen. The calculated contribution of the Yb subsystem to the heat capacity, shown by curve 1, follows the behavior of the $C_p/T(T)$ curve at $T < T_R$ in the state represented by Fig. 10(b) at $B = 0$. At $T > T_R$, the contribution of the Yb subsystem coincides with the curve C_p/T vs T in the state shown in Fig. 10(a) (curve 2). Thus, the calculations attribute the Schottky anomaly in C_p/T vs (T) dependence to the contribution of the Yb subsystem. This contribution is associated with redistribution of the levels population in the ground doublet of the Yb^{3+} ion split by the *f-d* interaction. The calculated splitting of the ground doublet of the Yb^{3+} ion due to the *f-d* interaction at $T = 2$ K is $\Delta_0 \approx 15\,cm^{-1}$. At T_R, it decreases abruptly to $\Delta_0 \approx 1.37\,cm^{-1}$. Such a change in the value of Δ_0 corresponds to the data of infrared spectroscopy.

VIII. CONCLUSIONS

Every member of the francisite family reveals new features in the behavior of these versatile compounds. This is true, in particular, for the rare-earth-substituted ones. The interplay of the rare-earth and transition-metal subsystems results in an additional phase transition taking place within a magnetically ordered state of rare-earth francisites. The details of this transition are sensitive to the species of rare-earth ions. In the present work, we found that the spin-reorientation phase transition in $Cu_3Yb(SeO_3)_2O_2Cl$ is of the first order in variance with the earlier observed second-order phase transition in $Cu_3Sm(SeO_3)_2O_2Cl$. We attempted a description of the thermodynamic data on Yb francisite based on a CF model for the Yb^{3+} ion and on the mean-field approximation. The f-d coupling parameter has been determined and its value was found to be in good correspondence with the available data of infrared spectroscopy. Despite the fact that the theoretical approach used has a limited applicability and did not allow quantifying the parameters of the d-d exchange, we found it capable to analyze the possible magnetic structures realized in $Cu_3Yb(SeO_3)_2O_2Cl$.

ACKNOWLEDGMENTS

We are grateful to R. M. Eremina for the valuable discussions concerning ESR data analysis. The work was supported by the Ministry of Education and Science of the Russian Federation in the framework of the Increase Competitiveness Program of NUST "MISiS" project K2-2016-066 and by RFBR projects 15-05-06742, 16-02-00021, 17-02-00211, and 17-52-45014. The work has been supported by Act 211 of the Government of Russian Federation, Contracts No. 02.A03.21.0004 and No. 02.A03.21.0011.

[1] A. Pring, B. M. Gatehouse, and W. D. Birch, Am. Mineral. **75**, 1421 (1990).
[2] P. Millet, B. Bastide, V. Pashchenko, S. Gnatchenko, V. Gapon, Y. Ksari, and A. Stepanov, J. Mater. Chem. **11**, 1152 (2001).
[3] P. Millet, M. Johnsson, V. Pashchenko, Y. Ksari, A. Stepanov, and F. Mila, Solid State Ionics **141-142**, 559 (2001).
[4] R. Berrigan and G. M. Gatehouse, Acta Crystallogr., Sect. C: Struct. Chem. **52**, 496 (1996).
[5] M. Pregelj, O. Zaharko, A. Günther, A. Loidl, V. Tsurkan, and S. Guerrero, Phys. Rev. B **86**, 144409 (2012).
[6] I. Rousochatzakis, J. Richter, R. Zinke, and A. A. Tsirlin, Phys. Rev. B **91**, 024416 (2015).
[7] S. A. Nikolaev, V. V. Mazurenko, A. A. Tsirlin, and V. G. Mazurenko, Phys. Rev. B **94**, 144412 (2016).
[8] D. A. Prishchenko, A. A. Tsirlin, V. Tsurkan, A. Loidl, A. Jesche, and V. G. Mazurenko, Phys. Rev. B **95**, 064102 (2017).
[9] E. Constable, S. Raymond, S. Petit, E. Ressouche, F. Bourdarot, J. Debray, M. Josse, O. Fabelo, H. Berger, S. deBrion, and V. Simonet, Phys. Rev. B **96**, 014413 (2017).
[10] H. C. Wu, K. D. Chandrasekhar, J. K. Yuan, J. R. Huang, J.-Y. Lin, H. Berger, and H. D. Yang, Phys. Rev. B **95**, 125121 (2017).
[11] R. Becker and M. Johnsson, Solid State Sci. **7**, 375 (2005).
[12] K. V. Zakharov, E. A. Zvereva, E. S. Kuznetsova, P. S. Berdonosov, V. A. Dolgikh, M. M. Markina, A. V. Olenev, A. A. Shakin, O. S. Volkova, and A. N. Vasiliev, J. Alloy Compd. **685**, 442 (2016).
[13] M. M. Markina, K. V. Zakharov, E. A. Zvereva, R.S. Denisov, P. S. Berdonosov, V. A. Dolgikh, E. S. Kuznetsova, A. V. Olenev, and A. N. Vasiliev, Phys. Chem. Miner. **44**, 277 (2017).
[14] K. V. Zakharov, E. A. Zvereva, P. S. Berdonosov, E. S. Kuznetsova, V. A. Dolgikh, L. Clark, C. Black, P. Lightfoot, W. Kockelmann, Z. V. Pchelkina *et al.*, Phys. Rev. B **90**, 214417 (2014).
[15] K. V. Zakharov, E. A. Zvereva, M. M. Markina, M. I. Stratan, E. S. Kuznetsova, S. F. Dunaev, P. S. Berdonosov, V. A. Dolgikh, A. V. Olenev, S. A. Klimin *et al.*, Phys. Rev. B **94**, 054401 (2016).
[16] P. S. Berdonosov and V. A. Dolgikh, Russ. J. Inorg. Chem. **53**, 1353 (2008).
[17] V. Petricek, M. Dusek, and L. Palatinus, Z. Kristallogr. **229**, 345 (2014).
[18] S. A. Altshuler and B. M. Kozyrev, *Electron Paramagnetic Resonance* (Academic, New York, 1964).
[19] A. V. Koshelev, E. A. Zvereva, D. A. Chareev, O. S. Volkova, A. Vymazalova, F. Laufek, E. V. Kovalchuk, B. Rahaman, T. Saha-Dasgupta, and A. N. Vasiliev, Phys. Chem. Miner. **43**, 43 (2016).
[20] R. M. Krishna and S. K. Gupta, Bull. Magn. Res. **16**, 239 (1994).
[21] K. Kawasaki, Prog. Theor. Phys. **39**, 285 (1968); Phys. Lett. A **26**, 543 (1968).
[22] H. Mori and K. Kawasaki, Prog. Theor. Phys. **28**, 971 (1962).
[23] D. L. Huber, Phys. Rev. B **6**, 3180 (1972).
[24] E. A. Zvereva, M. I. Stratan, Y. A. Ovchenkov, V. B. Nalbandyan, J.-Y. Lin, E. L. Vavilova, M. F. Iakovleva, M. Abdel-Hafiez, A. V. Silhanek, X.-J. Chen *et al.*, Phys. Rev. B **92**, 144401 (2015).
[25] P. M. Richards, Solid State Commun. **13**, 253 (1973).
[26] A. G. Anders and S. V. Volotski, J. Magn. Magn. Mater. **31-34**, 1169 (1983).
[27] M. N. Popova, S. A. Klimin, R. Troc, and Z. Bukowski, Solid State Commun. **102**, 71 (1997).
[28] E. A. Popova, S. A. Klimin, M. N. Popova, R. Klingeler, N. Tristan, B. Büchner, and A. N. Vasiliev, J. Magn. Magn. Mater. **331**, 133 (2013).
[29] S. A. Klimin, A. S. Galkin, and M. N. Popova, Phys. Lett. A **376**, 1861 (2012).
[30] K. P. Belov, A. K. Zvezdin, A. M. Kadomtseva, and R. Z. Levitin, Sov. Phys. Usp. **19**, 574 (1976).
[31] E. A. Popova, D. V. Volkov, A. N. Vasiliev, A. A. Demidov, N. P. Kolmakova, I. A. Gudim, L. N. Bezmaternykh, N. Tristan, Yu. Skourski, B. Büchner *et al.*, Phys. Rev. B **75**, 224413 (2007).
[32] C. Ritter, A. I. Pankrats, A. A. Demidov, D. A. Velikanov, V. L. Temerov, and I. A. Gudim, Phys. Rev. B **91**, 134416 (2015).
[33] A. A. Demidov, I. A. Gudim, and E. V. Eremin, Physica B **407**, 393 (2012).
[34] M. N. Popova, S. A. Klimin, E. P. Chukalina, B. Z. Malkin, R. Z. Levitin, B. V. Mill, and E. Antic-Fidancev, Phys. Rev. B **68**, 155103 (2003).